AIP Advances

Chalcogen-hyperdoped germanium for short-wavelength infrared photodetection

Cite as: AIP Advances **10**, 075028 (2020); https://doi.org/10.1063/5.0008281
Submitted: 20 March 2020 . Accepted: 23 June 2020 . Published Online: 30 July 2020

Hemi H. Gandhi, David Pastor, Tuan T. Tran, Stefan Kalchmair, Lachlan A. Smillie, Jonathan P. Mailoa, Ruggero Milazzo, Enrico Napolitani, Marko Loncar, James S. Williams, Michael J. Aziz, and Eric Mazur

Chalcogen-hyperdoped germanium for short-wavelength infrared photodetection

Cite as: AIP Advances 10, 075028 (2020); doi: 10.1063/5.0008281
Submitted: 20 March 2020 • Accepted: 23 June 2020 •
Published Online: 30 July 2020

Hemi H. Gandhi,[1,a] David Pastor,[1,2,a] Tuan T. Tran,[3,4] Stefan Kalchmair,[1] Lachlan A. Smillie,[3] Jonathan P. Mailoa,[4,5] Ruggero Milazzo,[6] Enrico Napolitani,[6] Marko Loncar,[1] James S. Williams,[3] Michael J. Aziz,[1,a] and Eric Mazur[1,a]

AFFILIATIONS

[1]Harvard John A. Paulson School of Engineering and Applied Sciences, Cambridge, Massachusetts 02138, USA
[2]Departamento de Estructura de la Materia, Física térmica y Electrónica, Facultad de Ciencias Físicas, 28040 Madrid, Spain
[3]Department of Electronic Materials Engineering, Research School of Physics and Engineering, Australian National University, Canberra, ACT 0200, Australia
[4]Department of Physics and Astronomy, Ångström Laboratory, Uppsala University, P.O. Box 516, SE-751 20 Uppsala, Sweden
[5]Robert Bosch LLC, Cambridge, Massachusetts 02138, USA
[6]Dipartimento di Fisica e Astronomia, Università di Padova and CNR-IMM, Via Marzolo 8, I-35131 Padova, Italy

[a]**Authors to whom correspondence should be addressed:** hemi.gandhi@alumni.harvard.edu; dpastor@fis.ucm.es; maziz@harvard.edu; and mazur@seas.harvard.edu

ABSTRACT

Obtaining short-wavelength-infrared (SWIR; 1.4 μm–3.0 μm) room-temperature photodetection in a low-cost, group IV semiconductor is desirable for numerous applications. We demonstrate a non-equilibrium method for hyperdoping germanium with selenium or tellurium for dopant-mediated SWIR photodetection. By ion-implanting Se or Te into Ge wafers and restoring crystallinity with pulsed laser melting induced rapid solidification, we obtain single crystalline materials with peak Se and Te concentrations of 10^{20} cm^{-3} (10^4 times the solubility limits). These hyperdoped materials exhibit sub-bandgap absorption of light up to wavelengths of at least 3.0 μm, with their sub-bandgap optical absorption coefficients comparable to those of commercial SWIR photodetection materials. Although previous studies of Ge-based photodetectors have reported a sub-bandgap optoelectronic response only at low temperature, we report room-temperature sub-bandgap SWIR photodetection at wavelengths as long as 3.0 μm from rudimentary hyperdoped Ge:Se and Ge:Te photodetectors.

I. INTRODUCTION

Short-wavelength-infrared (SWIR) (1 μm–3 μm) photodetection is used for numerous commercial, military, and scientific applications.[1–4] Conventional semiconductors such as silicon and germanium, however, do not absorb and detect SWIR photons, which have an energy below that of the intrinsic bandgap of these materials. Current state-of-the-art SWIR photodetectors are made from narrow bandgap III-V or II-VI semiconductors (e.g., InGaAs, InAs, $Pb_{1-x}Se_x$, and $Hg_{1-x}Cd_xTe$) that are heterogeneously integrated with Si-CMOS electronics.[1,4,5] Three main issues constrain the applicability of photodetectors made in this manner. First, III-V and II-VI semiconductors are chemically incompatible with Si-CMOS processing, limiting the size of final photodetector focal plane arrays, and are often expensive or toxic.[1,5,6] Second, their heterogeneous integration is a complex, low-throughput process that further increases final device cost. Third, photodetectors made from the majority of these materials must be cooled to low temperature to attain satisfactory signal-to-noise ratios. The lack of a low-cost, non-toxic material capable of room-temperature SWIR photodetection limits applications involving SWIR photodetection.

An alternative to using III-V or II-VI materials is to induce a low-cost, Si-compatible material such as germanium to detect SWIR-light through dopant-mediated photoconductivity. In this

paper, we report dopant-mediated sub-bandgap photodetection in Ge doped with supersaturated concentrations of Se or Te. We fabricate these materials using a scalable, non-equilibrium hyperdoping method, consisting of ion implantation of Se or Te into Ge followed by nanosecond pulsed laser melting (PLM) induced rapid solidification. This hyperdoping process produces single-crystal materials with peak Se and Te dopant concentrations of 10^{20} cm^{-3}, which are four orders of magnitude above the Ge:Se and Ge:Te solubility limits. The hyperdoping increases the dopant-mediated sub-bandgap absorption coefficients α of these materials to values comparable to those of commercial SWIR III-V and II-VI materials. We test rudimentary photodetectors made from hyperdoped Ge:Se and Ge:Te for sub-bandgap optoelectronic response and demonstrate that these materials can be used for room-temperature sub-bandgap photodetection.

While recent sub-bandgap photodetection studies have focused on Si, we work with Ge because of its higher carrier mobility.[7–12] Previous studies of dopant-mediated Ge photodetectors incorporating different dopants (S, Te, Zn, B, Cu, Cd, Zn, and Au) through various doping methods have reported sub-bandgap response only at low temperature, which is impractical for many SWIR applications.[13–17] In this paper, we chose Se and Te as dopants because they are deep-level-dopants[18] (supplementary material Fig. 1), and among deep-level Ge-dopants, they have relatively high equilibrium solubility limits.[19,20] Compared to Ge with shallow-level dopants, Ge doped with deep-level-dopants demonstrates lower thermal ionization at room-temperature, reducing background free-carrier concentrations and improving device signal-to-noise ratios.[13,14] A higher equilibrium solubility limit permits attaining even higher concentrations through hyperdoping,[21] leading to a higher sub-bandgap absorption coefficient.[13,14]

II. EXPERIMENTAL FABRICATION AND CHARACTERIZATION

To fabricate chalcogen-hyperdoped Ge, we first implant *p*-type (100) Ge wafers of 5 Ω cm–10 Ω cm resistivity with either 60-keV $^{80}Se^{+}$ ions or 80-keV $^{130}Te^{+}$ ions to a dose of either 10^{14} cm^{-2} or 10^{15} cm^{-2}. The projected range for both doses is 27 nm. We performed all implantations at liquid-nitrogen temperature to suppress ion-beam-induced porosity and dynamic annealing. During implantation, all substrates were oriented 7° with respect to the [100] crystal axis to minimize ion channeling.

To characterize the resulting amorphous layer, we performed channeling Rutherford backscattering spectrometry (RBS) on the samples with a 2-MeV He^{+} ion beam aligned along the [100] axis. We used the SIMNRA program to simulate the RBS spectra (supplementary material Figs. 3 and 4). After implantation, the 10^{14}-cm^{-2} and 10^{15}-cm^{-2} dose samples have an amorphous-layer thickness of 60 nm and 75 nm for Se samples and 60 nm and 76 nm for the Te samples, respectively, as measured by RBS. To restore crystallinity after implantation damage, we laser-melted each sample with a 355-nm, 0.49-J/cm^2, single 4-ns FWHM pulse from a Nd:YAG laser [supplementary material Fig. 2(a)].

We chose this fluence to reach a melt depth of 210 nm (predicted by numerical solutions to the heat equation), which is expected to be safely beyond the deep tail of the implant distribution and beyond the implant-amorphized and implant-damaged regions of each sample [supplementary material Fig. 2(d)].[22] Under this scenario, the melt front reaches the underlying perfect crystalline substrate, permitting defect-free single-crystal epitaxial regrowth. During PLM, time-resolved reflectivity measurements indicate the following melt durations: 33 ns–54 ns for the 10^{14}-cm^{-2} samples and 39 ns–66 ns for the 10^{15}-cm^{-2} samples. These measured melt-durations are consistent with numerical simulations [supplementary material Fig. 2(b)].

To measure Se and Te concentration–depth profiles, we carried out secondary ion mass spectrometry using a 5.5-keV Cs^{+} ion beam and collected $^{133}Cs^{80}Se^{+}$ and $^{133}Cs^{130}Te^{+}$ secondary ions, respectively. To examine the impact of PLM on sub-surface implantation damage, we carried out bright-field and high-resolution cross-sectional transmission electron microscopy (XTEM) at 200 keV. We prepared the samples for XTEM using a focused ion beam and *in situ* lift-out. To quantify absorptance, we measured transmittance (T) and reflectance (R) using a UV-VIS-NIR spectrophotometer and a Fourier-transform infrared spectrometer (FTIR). To minimize gas-absorption lines in absorptance data, we purged the FTIR chamber with liquid nitrogen before all measurements.

To test whether chalcogen-hyperdoped Ge exhibits room-temperature sub-bandgap optoelectronic response, we fabricated rudimentary photodetectors using 10^{15}-cm^{-2} dose hyperdoped samples. We created a bottom contact to the *p*-type wafer substrate by thermally evaporating a 200-nm thick Al-layer. On the wafer side opposite the Al back-contact, we formed an *n*++ Ge:Se or Ge:Te layer via the hyperdoping process detailed above. Using photolithography and SF_6 reactive ion etching, we then formed a mesa structure out of the *n*++ layer to electrically isolate the region from the rest of the substrate. The mesas were 4 μm deep and 1 × 1 mm^2 in area. We then used photolithography, e-beam evaporation, and lift-off to form 200-nm thick Ni-bar contacts on opposite sides of the mesa structure (separated 1000 μm apart) to create the top photodetector device contacts. All contacts were Ohmic. We attached the bottom contact to a printed circuit board (PCB) with silver paste and wire-bonded the top contacts to the PCB. All photodetectors rectified when current was passed between the top and bottom contacts.

We tested the photodetectors using a 2.0-μm laser photoconductivity setup. We illuminated the photodetectors with chopped light from a continuous-wave laser diode (Brolis semiconductor) at a wavelength of 2.0 μm. The laser light was mechanically chopped at 23 Hz and focused on a 20-μm spot size in the middle of the mesa-structure surface. Using a lock-in amplifier, we measured the AC current generated between the photodetector's two top-bar-contacts and the bottom-contact.

To determine the spectral photoresponse of the photodetectors, we substituted each detector in an FTIR spectrometer with a photodetector. In this FTIR photoconductivity setup, we connected a photodetector to a *trans*-impedance amplifier (TIA) for amplification of the photocurrent. No bias voltage was applied to the photodetector during measurement. The FTIR resolution was set to 100 cm^{-1}. To reduce noise, we set the band pass filter of the TIA to the 0.1 kHz to 10 kHz range. We obtained the photoconductive spectrum in arbitrary units since the incident power from the Globar was unknown. The measured photoresponse of each detector was normalized to the emission spectrum of the Globar light source. When measuring dark noise, we blocked the illumination from the FTIR

spectrometer just before the objective lens to ensure that no light reached the photodetector.

III. RESULTS AND DISCUSSION

A. Chalcogen dopant-profile

Figures 1(a) and 1(b) show the Ge:Se and Ge:Te concentration depth profiles, respectively, of the low (10^{14} cm^{-2}) and high (10^{15} cm^{-2}) dose samples before and after laser melting, obtained by secondary ion mass spectrometry. The as-implanted concentration depth profiles each have an expected Gaussian-like shape. In the laser-melted hyperdoped samples, the Se and Te concentration–depth profiles are still Gaussian-like but have undergone some impurity redistribution compared to the as-implanted profiles. This broadening in concentration–depth profiles after laser melting is characteristic of liquid-phase impurity diffusion in the melt. We interpret the surface spikes in the first 10 nm of all the profiles as SIMS surface-transient measurement artifacts.[23] The noisy concentration signals below 5×10^{17} cm^{-3} in the Se profile and below 1×10^{17} cm^{-3} for Te profile reflect the SIMS sensitivity limit. All four laser-melted samples shown in Figs. 1(a) and 1(b) have supersaturated dopant concentrations. The peak Se concentration in the high-dose laser-melted hyperdoped sample, 1×10^{20} cm^{-3}, is four orders of magnitude larger than the Ge:Se solubility limit[19] of 5×10^{15} cm^{-3}. Likewise, the peak Te concentration in the high-dose laser-melted hyperdoped sample, 1×10^{20} cm^{-3}, is four orders of magnitude larger than the Ge:Te solubility limit[19] of 2×10^{15} cm^{-3}. We confirmed that Te was substitutional in the Ge lattice following PLM using RBS and channeling. We can estimate the retained impurity-doses after PLM by comparing integrations of the SIMS profiles before and after PLM. For these estimations, we integrate the dopant profile of each sample from a depth of 10 nm to the depth at which each profile reaches the respective SIMS sensitivity limit. We begin integrating from 10 nm because of artifacts in the SIMS measurement near the sample surface. These integrations indicate that in the Se samples, after PLM, 67 ± 5% of the as-implanted low-dose and 84 ± 5% of the as-implanted high-dose are retained. For the Te samples, 71 ± 5% of the as-implanted low-dose and 90 ± 5% of the as-implanted high-dose are retained after PLM.

B. Crystal structure

Figures 2(a) and 2(b) show XTEM and HRXTEM (inset) micrographs of the high-dose hyperdoped Ge:Se and Ge:Te samples, respectively. The Se and Te micrographs appear very similar and exhibit the same essential features. The micrographs show that the bulk of each sample is single-crystalline. No extended defects, secondary phases, or cellular breakdown features are visible in either micrograph. The hyperdoped layer thicknesses, evaluated by SIMS, of the laser melted Se and Te samples are 105 nm and 115 nm, respectively. For each sample, the hyperdoped layer appears identical to the substrate beneath. The micrographs demonstrate that pulsed laser melting fully restores the crystallinity of the implantation-damaged region.

Three other features of the micrographs are worth noting. First, both samples exhibit an amorphous looking surface layer that is characteristic of a surface oxide layer obtained after PLM. Second, the interface between the amorphous surface layer and the bulk regions contains small, diffuse dark regions. We suspect these regions are bend contrast that arises due to localized strain produced by localized dopant-concentration peaks at the surface. We note that the high-resolution imaging and selected area diffraction yield no evidence of crystallites which might otherwise be responsible for such features. Third, spots are visible throughout each micrograph that are characteristic of focused-ion-beam-induced damage in Ge.[24,25] Because these spots are found throughout the specimen (well beyond the hyperdoped layers), we conclude that they do not arise from the hyperdoping process.

C. Sub-bandgap absorptance

Figure 3(a) shows the difference between the sub-bandgap absorptance ($A = 1 - T - R$) of hyperdoped Ge:Se and Ge:Te and that of a virgin Ge wafer, $A_{\mathrm{HypGe}} - A_{\mathrm{Ge}}$. Both high-dose samples and the low-dose Te samples exhibit significant sub-bandgap absorptance, whereas the low-dose Se sample does not. The sub-bandgap absorptance of each sample is relatively constant over the 2 μm–3 μm region shown. Among the samples, the high-dose Se sample exhibits the largest sub-bandgap absorptance. For both Ge:Se and Ge:Te, the sub-bandgap absorptance increases with implant dose. In Fig. 3(b), we show the αd product of the samples with sub-bandgap absorptance. By modeling each sample as a two-layer thin-film absorbing stack,[7] we estimate the product of the absorbing layer thickness, d, and the absorption coefficient, α, from the data in Fig. 3(a). In this estimate, we assume hyperdoped samples have a reflection coefficient at 2.4 μm equivalent to that of a virgin-Ge-air interface (0.366 at 2.4 μm). Further assuming that the hyperdoped layer in each sample uniformly absorbs sub-bandgap light, we obtain the following α

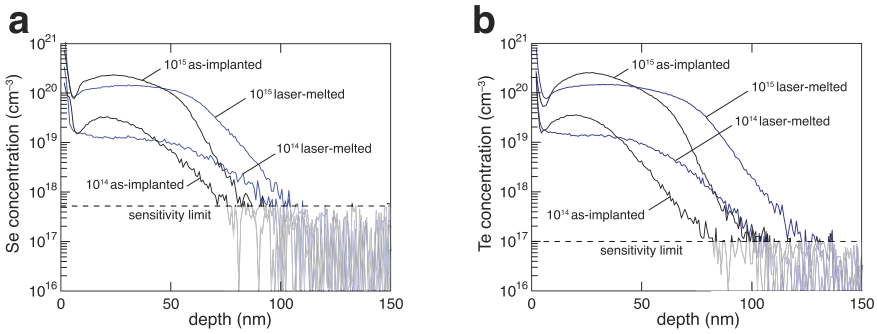

FIG. 1. SIMS concentration–depth profiles of implanted Ge wafers with (a) 60-keV Se ions to a dose of 10^{14} cm^{-2} or 10^{15} cm^{-2} and (b) 80-keV Te ions to a dose of 10^{14} cm^{-2} or 10^{15} cm^{-2}, followed by laser melting at 0.49 J/cm^2. Laser-melted, hyperdoped samples have peak dopant concentrations four orders of magnitude higher than their respective solubility limits.

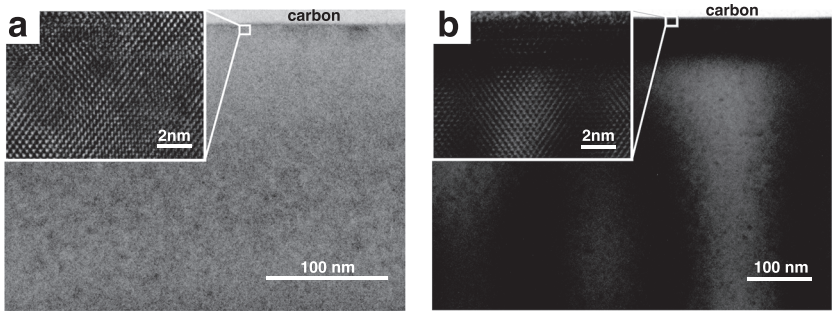

FIG. 2. Cross-sectional TEM and HRTEM (inset) micrographs of 10^{15} cm^{-2} dose, 0.49 J/cm^2 laser-melted hyperdoped (a) Ge:Se and (b) Ge:Te samples.

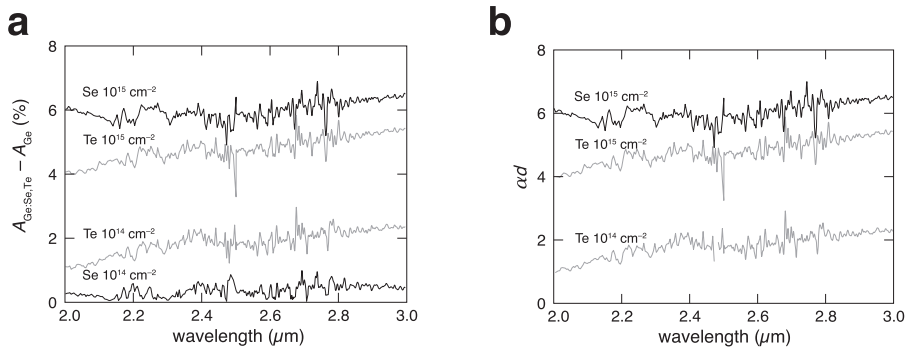

FIG. 3. (a) Difference between the sub-bandgap absorptance ($A = 1 - T - R$) of hyperdoped Ge:Se and Ge:Te and that of a virgin Ge wafer, $A_{HypGe} - A_{Ge}$. Samples were laser-melted with a 0.49 J/cm^2 fluence. The crossover between the spectrophotometer and FTIR spectrometer measurements is at 2.5 μm. The 10^{14} cm^{-2} dose Te and 10^{15} cm^{-2} dose Se and Te samples show sub-bandgap absorptance and (b) the calculated αd product (left axis) for the three hyperdoped samples that show sub-bandgap absorptance.

values at a wavelength of 2.4 μm: α = 1300 cm^{-1} for a 10^{19} cm^{-3} effective concentration (for low-dose Te, taking the layer thickness to be 100 nm), α = 5000 cm^{-1} for a 10^{20} cm^{-3} effective concentration (for high-dose and a Se thickness of 100 nm), and α = 3700 cm^{-1} for a 8.3 × 10^{19} cm^{-3} effective concentration (for high-dose Te and a thickness of 120 nm). These sub-bandgap α values are comparable to those of commercially available direct-bandgap semiconductors used for SWIR photodetection at the same wavelength.[26] Estimated wavelength-dependent αd products of each sample, calculated from estimates of α and d described above, are presented in Fig. 3(b).

D. Sub-bandgap optoelectronic response

Figure 4(a) shows the setup for measuring the response of the photodetectors made from chalcogen-hyperdoped Ge under 2.0-μm laser light. In the planar-device structure shown in the figure, the chalcogen-hyperdoped layer sits atop a raised mesa structure. We chose this planar-device structure for its simplicity and potential suitability for SWIR-imaging-array applications. The hyperdoped-layer atop the mesa is isolated from the substrate to reduce leakage currents and to ensure that any applied voltage passes through the device's p-n++ junction. In each photodetector, the hyperdoped layer forms a rectifying junction with the p-type substrate, as shown in the dark I–V curve in Fig. 4(b). Figure 4(c) shows the difference between the I–V curves obtained under 2.0-μm laser illumination and no illumination. This photocurrent difference demonstrates sub-bandgap photocurrent. Increasing reverse bias across the junction increases (and then saturates) sub-bandgap photocurrent due to enhanced collection of charge carriers excited by the sub-bandgap light. Under zero bias voltage and 2.0-μm illumination at room temperature, the Ge:Se and Ge:Te photodetectors exhibit an external quantum efficiency (EQE) of 1.0 × 10^{-5} and 6.0 × 10^{-5}, respectively. The low EQE of these initial rudimentary devices can be increased straightforwardly by optimizing hyperdoping fabrication to enhance sub-bandgap absorptance (i.e., the αd product) and by increasing photon and carrier collection through improved device design and fabrication.

Figure 4(d) shows the broadband response of the chalcogen-hyperdoped photodetectors, obtained by substituting each detector in the FTIR spectrometer with a hyperdoped photodetector. The response of each detector is normalized to the intensity spectrum of the FTIR Globar. Because we do not know the incident power per unit wavelength of the FTIR Globar illuminating the photodetectors and because the response is obtained from a Fourier transform of the phase-corrected time-domain interferogram, we report the normalized photoconductive response in arbitrary units. Between 2.2 μm and 3.0 μm, the response of the hyperdoped Ge:Se is consistently larger than that of the Ge:Te photodetector. We note that the 10^{15} cm^{-2}-dose hyperdoped Ge:Se sample also shows higher

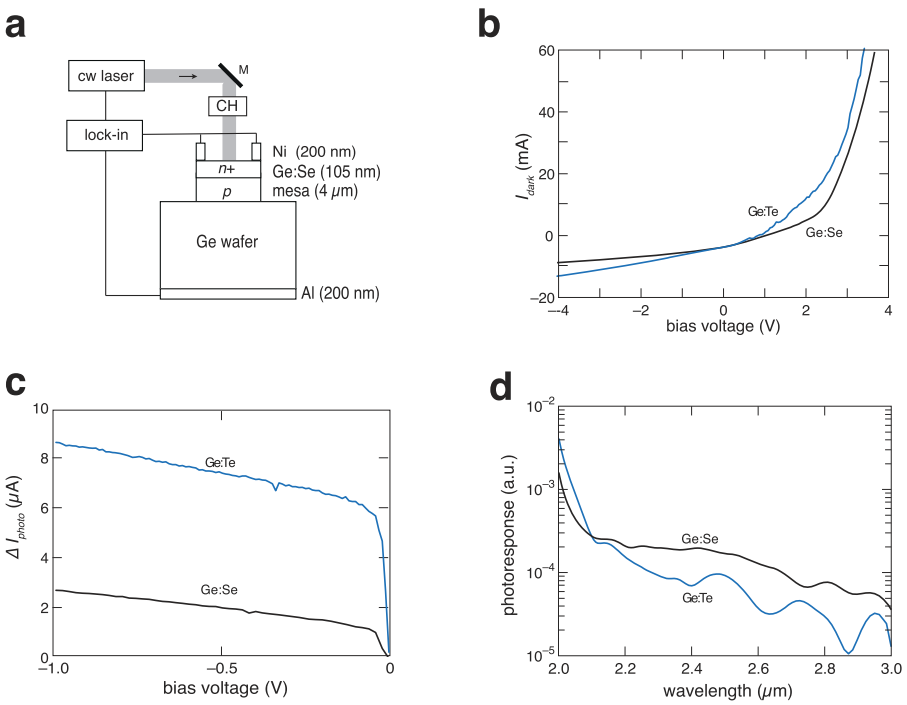

FIG. 4. (a) Schematic of the 2.0-μm laser photoconductivity setup for measuring the optoelectronic response of the hyperdoped germanium photodetectors. The optically active region of each photodetector consists of 10^{15} cm^{-2} dose, 0.49 J/cm^2 laser-melted hyperdoped material, (b) the photodetectors' dark I–V curve, (c) the difference between the photodetectors' 2.0-μm-laser illuminated and dark I–V curve, (d) measured broadband room-temperature photoresponse of photodetectors at zero bias, obtained by substituting each detector in an FTIR spectrometer with a photodetector and illuminating with Globar light. The response of each detector is normalized to the intensity spectrum of the FTIR Globar.

sub-bandgap absorptance between 2.2 μm and 3.0 μm than the Ge:Te sample (Fig. 2). The dark noise for the Ge:Se and Ge:Te photodetectors is 1.0×10^{-5} and 2.0×10^{-5}, respectively. The Ge:Se and Ge:Te photodetectors both exhibit a room-temperature, sub-bandgap response out to wavelengths beyond the detection edge of extended InGaAs, which has a bandgap of 2.6 μm.

IV. CONCLUSION

Chalcogen-hyperdoped Ge exhibits room-temperature SWIR photodetection. Ion implantation, followed by pulsed laser melting induced rapid solidification, produces single crystal materials with peak Se and Te concentrations of 10^{20} cm^{-3} (10^4 times the Ge:Se and Ge:Te solubility limits). We estimate that 10^{15}-cm^{-2} dose hyperdoped Ge:Se and Ge:Te samples have an average sub-bandgap absorption coefficient at λ = 2.4 μm of 5000 cm^{-1} and 3700 cm^{-1}, respectively, which is comparable to those of commercial materials at the same wavelength. Rudimentary photodetectors made of hyperdoped Ge:Se exhibit a room-temperature optoelectronic response between 2.0 μm and 3.0 μm, which is consistently higher than that of hyperdoped Ge:Te photodetectors between 2.2 μm and 3.0 μm. These results suggest that chalcogen-hyperdoped Ge has the potential to be used for low-cost, room-temperature, silicon-compatible SWIR-photodetection.

SUPPLEMENTARY MATERIAL

Additional figures are presented in the supplementary material: Ge:Se and Ge:Te energy-defect levels, laser-melting setup and simulations, Ge:Se RBS spectra, and Ge:Te RBS spectra.

AUTHORS' CONTRIBUTIONS

H.H.G. and D.P. are the co-first authors and contributed equally to this work. H.H.G. and D.P. proposed the initial concept for the study. H.H.G., D.P., T.T.T., J.S.W., M.J.A., and E.M. designed the hyperdoping experiments. D.P. performed PLM melting simulations. D.P. and T.T.T. performed SRIM calculations. T.T.T. and J.S.W. performed implantations and RBS measurements. D.P. and H.H.G. performed PLM. D.P., H.H.G., and J.P.M. performed absorptance measurements. T.T.T., E.N., and R.M. performed SIMS measurements. L.A.S. performed XTEM measurements. J.P.M., D.P., and H.H.G. finalized the photodetector-device design. D.P. and H.H.G. fabricated the photodetectors. S.K. and D.P. performed photoconductivity experiments. H.H.G. prepared the manuscript. H.H.G., D.P., and T.T.T. prepared the manuscript figures. E.M. and M.J.A., supervised the work and development of the manuscript.

ACKNOWLEDGMENTS

H.H.G. acknowledges support from the Department of Defense (DoD), under Grant No. DGE 0946799, through the National Defense Science and Engineering Graduate Fellowship (NDSEG) Program, the Harvard University Frank Knox Memorial Traveling Fellowship, and the Directed Energy Processing Society Graduate Fellowship. D.P. acknowledges financial support from the MEC within Programa Nacional de Movilidad de Recursos Humanos del Plan Nacional I+D+i 2008–2011 (Grant No. EX-2010-0662), the Ramón y Cajal Program (Grant No. RYC-2014-16936), and the Spanish Ministry of Science, Innovation and Universities

(MICINN), under Contract No. TEC2017-84378-R. This work was also supported by the U.S. Air Force Office of Scientific Research (Grant No. FA9550-14-1-0150). This work was performed in part at the Harvard Center for Nanoscale Systems (CNS), a member of the National Nanotechnology Infrastructure Network (NNIN), which is supported by the National Science Foundation under NSF Award No. ECS-0335765. L.A.S. thanks Austin J. Akey for assistance with XTEM measurements. H.H.G. thanks Austin J. Akey, Meng-Ju Sher, Daniel Recht, and Mark Winkler for feedback throughout the experimental planning process. H.H.G. and D.P. thank Karl K. Berggren and Emily Toomey at MIT for assistance in wire-bonding.

DATA AVAILABILITY

The data that support the findings of this study are available from the corresponding author upon reasonable request.

REFERENCES

[1] M. P. Hansen and D. S. Malchow, Proc. SPIE **6939**, 693901 (2008).
[2] R. G. Driggers, V. Hodgkin, and R. Vollmerhausen, in *Infrared Imaging Systems: Design, Analysis, Modeling, and Testing XXIV*, edited by G. C. Holst and K. A. Krapels (SPIE, 2013), p. 87060L.
[3] M. Lothode, V. Carrere, and R. Marion, in *2014 IEEE Geoscience and Remote Sensing Symposium* (IEEE, 2014), pp. 3288–3291.
[4] A. Rogalski, Infrared Phys. Technol. **54**, 136 (2011).
[5] Y. Arslan, F. Oguz, and C. Besikci, Infrared Phys. Technol. **70**, 134 (2015).
[6] T. E. Kazior, Philos. Trans. R. Soc., A **372**, 20130105 (2014).
[7] J. P. Mailoa, A. J. Akey, C. B. Simmons, D. Hutchinson, J. Mathews, J. T. Sullivan, D. Recht, M. T. Winkler, J. S. Williams, J. M. Warrender, P. D. Persans, M. J. Aziz, and T. Buonassisi, Nat. Commun. **5**, 3011 (2014).
[8] M. Casalino, G. Coppola, R. M. De La Rue, and D. F. Logan, Laser Photonics Rev. **10**, 895 (2016).
[9] J. J. Ackert, D. J. Thomson, L. Shen, A. C. Peacock, P. E. Jessop, G. T. Reed, G. Z. Mashanovich, and A. P. Knights, Nat. Photonics **9**, 393 (2015).
[10] S. Q. Lim, C. T.-K. Lew, P. K. Chow, J. M. Warrender, J. S. Williams, and B. C. Johnson, J. Appl. Phys. **126**, 224502 (2019).
[11] W. Yang, Q. Hudspeth, P. K. Chow, J. M. Warrender, N. Ferdous, E. Ertekin, G. Malladi, A. J. Akey, M. J. Aziz, and J. S. Williams, Phys. Rev. Appl. **12**, 024015 (2019).
[12] W. Yang, N. Ferdous, P. J. Simpson, J. M. Gaudet, Q. Hudspeth, P. K. Chow, J. M. Warrender, A. J. Akey, M. J. Aziz, E. Ertekin, and J. S. Williams, APL Mater. **7**, 101124 (2019).
[13] E. H. Putley, Phys. Status Solidi B **6**, 571 (1964).
[14] N. Sclar, Prog. Quantum Electron. **9**, 149 (1984).
[15] J. Bandaru, J. W. Beeman, E. E. Haller, S. Samperi, and N. M. Haegel, Infrared Phys. Technol. **43**, 353 (2002).
[16] J. W. Beeman, S. Goyal, L. A. Reichertz, and E. E. Haller, Infrared Phys. Technol. **51**, 60 (2007).
[17] J. Zhu, H. Zhu, H. Xu, Z. Weng, and H. Wu, Infrared Phys. Technol. **92**, 13 (2018).
[18] H. G. Grimmeiss, L. Montelius, and K. Larsson, Phys. Rev. B **37**, 6916 (1988).
[19] N. K. Abrikosov, V. F. Bankina, L. V. Poretskaya, L. E. Shelimova, and E. V. Skudnova, *Semiconducting II–VI, IV–VI, and V–VI Compounds* (Springer, Moscow, 1969).
[20] *Germanium-Based Technologies: From Materials to Devices*, 1st ed., edited by C. Claeys and E. Simoen (Elsevier Science, Amsterdam, Boston, 2007).
[21] P. M. Smith and M. J. Aziz, Acta Metall. Mater. **42**, 3515 (1994).
[22] LIMP, for Laser Induced Melting Predictions, Is a Numerical Solution to the 1-D Heat Equation for PLM. It Was Originally Written by Michael O. Thompson and Modified by Jeffrey A. West, Patrick Michael Smith and David E. Hoglund. A Partial Description Can Be Found, in D. E. Hoglund, M. O. Thompson, and M. J. Aziz, "Experimental test of morphological stability theory for a planar interface during rapid solidification," Phys. Rev. B **58**, 189–199 (1998) (n.d.).
[23] R. G. Wilson, F. A. Stevie, and C. W. Magee, *Secondary Ion Mass Spectrometry: A Practical Handbook for Depth Profiling and Bulk Impurity Analysis* (Wiley, New York, 1989).
[24] N. Yao, *Focused Ion Beam Systems: Basics and Applications* (Cambridge University Press, 2007).
[25] S. Rubanov and P. R. Munroe, Micron **35**, 549 (2004).
[26] A. Rogalski, *Infrared Detectors* (CRC Press, 2010).

CHALCOGEN-HYPERDOPED GERMANIUM FOR SHORT-WAVELENGTH INFRARED PHOTODETECTION

SUPPLEMENTARY MATERIALS.

FIGURE LIST:

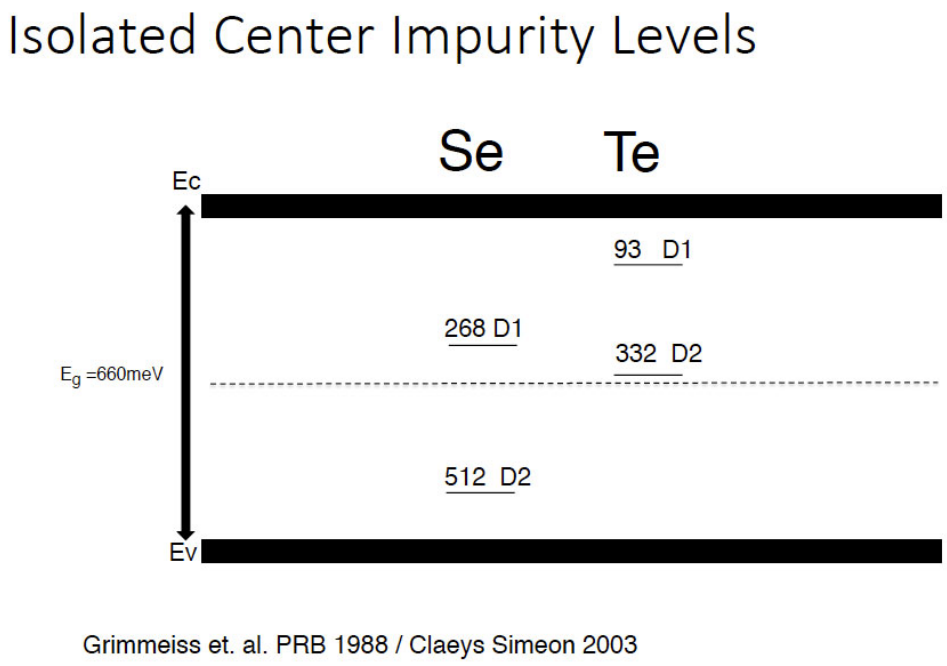

SM Figure1. **Ge:Se and Ge:Te defect levels.** At Ge:Se and Ge:Te concentrations below the solubility-limit, each dopant produces two donor defect states in Ge. At these lightly doped concentrations, the defect states are discrete and non-interacting. At these defect levels, photons with wavelengths of 4.62 and 2.42μm (and also shorter wavelength higher-energy photons) would be able to excite carriers from Ge:Se's D1 and D2 defect levels, respectively, to the conduction band. Similarly, photons with wavelengths of 13.3 and 3.73 μm (and also shorter wavelength, higher-energy photons) would be able to excite carriers from Ge:Te's D1 and D2 defect levels, respectively, to the conduction band. The Ge:Se D2 to conduction band photoconductive transition is within the measured absorption range in the

manuscript. At hyperdoped concentrations demonstrated in the manuscript, we expect the defect levels to interact and alter absorption features compared to lightly doped samples

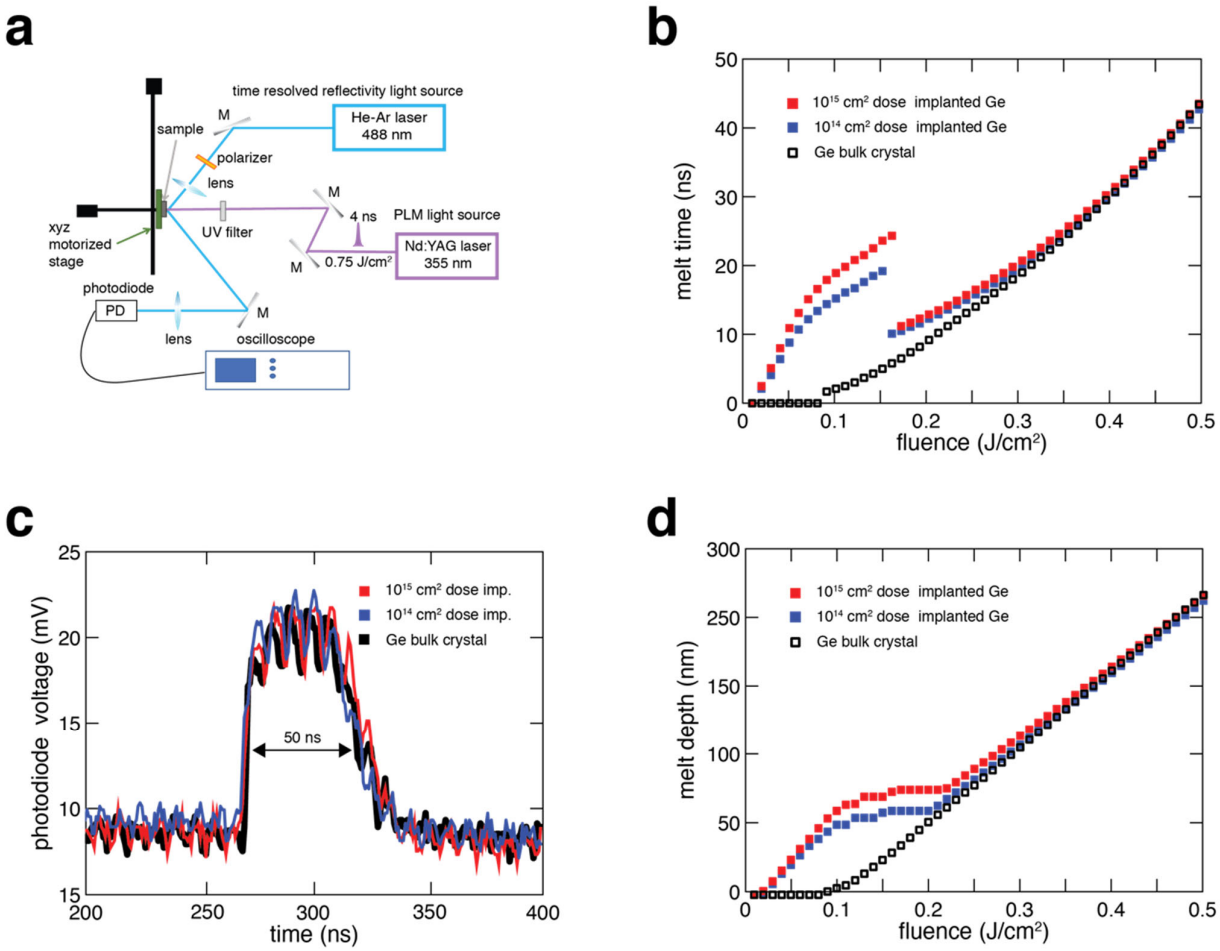

SM Figure2. Laser-melting setup and simulations.

a) In our experimental laser-melting set-up, we use time-resolved reflectivity (TRR), with a 488-nm probe laser-beam, to measure in-situ sample melt-durations. We compare measured melt-durations with melting simulations (numerical solutions to the heat equation) to understand sample melt dynamics
b) Fluence dependent melt-duration simulations of a virgin Ge bulk crystal wafer and implanted-Ge-wafer samples. The simulations assume a 4-ns 355-nm pulse from a Nd:YAG laser. The simulations also model the 10^{14} cm^{-2} and 10^{15} cm^{-2} dose implanted wafers as 60 and 75 nm thick amorphous-Ge layers, respectively, atop a crystalline Ge substrate. Modelled amorphous thicknesses are based off measured values from RBS (further discussed below). During PLM, time-resolved reflectivity measurements indicate the following melt durations: 33–54 ns for the 10^{14}-cm^{-2} samples, and 39–66 ns for the 10^{15}-cm^{-2} samples.
c) Characteristic TRR melt traces of a germanium bulk crystal wafer and 10^{15} cm^{-2} dose implanted wafers, melted with a fluence of 0.49-J/cm^2. During PLM, time-resolved

reflectivity measurements indicate the following melt durations: 33–54 ns for the 10^{14}-cm^{-2} samples, and 39–66 ns for the 10^{15}-cm^{-2} samples. These measured melt durations are consistent with values predicted in the simulation in figure b.

d) Fluence-dependent melt-depth simulations of crystalline Ge and implanted-Ge samples. Simulation assumptions are the same as in a. Simulations suggests that the melt-front, produced from a 0.49-J/cm^2 pulse, completely melts the measured 75-nm thick 10^{15} cm^{-2} implant-amorphized region and reaches the underlying crystalline substrate, leading to single-crystal epilayer regrowth.

RBS Measurements:

To characterize the resulting amorphous layer after implantation, we performed channelling Rutherford backscattering spectrometry (RBS) on the samples with a 2-MeV He^+ ion beam aligned along the [100] axis. We evaluated ion scattering measurements by simulating RBS spectra using the SIMNRA simulation program. The program, in general, considers only single scattering events allowing analytical formulae to be used for the calculation of the scattering parameters, which vastly speeds up the simulation. Also, we have chosen SRIM for the electronic stopping power data as SRIM is a semi-empirical database that relies on available experimental stopping power. For MeV ion scattering, the electronic energy loss provided by SRIM is very reproducible. RBS simulations of the implanted spectra indicate that the 10^{14}-cm^{-2} and 10^{15}-cm^{-2} dose samples have an amorphous-layer thickness of 60 and 75 nm for Se samples, and of 60 and 76 nm for the Te samples, respectively, as measured by RBS. As indicated in the Figure captions, the channelling spectra after PLM indicate excellent crystallinity with channelling minimum yields comparable to virgin Ge spectra. In the case of Te at a dose of 10^{15} cm^{-2} the substitutional Te fraction is at least 70%.

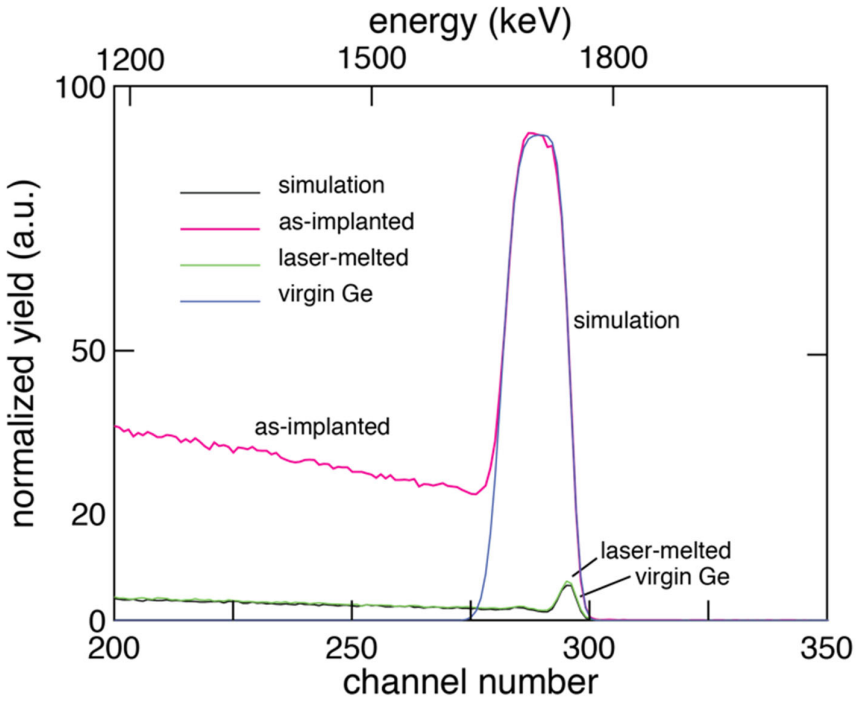

SM Figure 3. Ge:Se RBS spectra. Channelling-mode RBS spectra of a virgin-Ge wafer and of Se-implanted high-dose (10^{15} cm^{-2}) samples before and after PLM. RBS is not able to distinguish and detect Se, since the mass of Se is very similar to that of Ge and the Ge and Se parts of the spectra overlap. The minimum scattering yield of the laser-melted hyperdoped Ge:Se sample ($\chi_{min/Ge}$) is very close to that of the virgin Ge wafer, suggesting that the hyperdoped samples after laser-melting are of excellent crystalline quality.

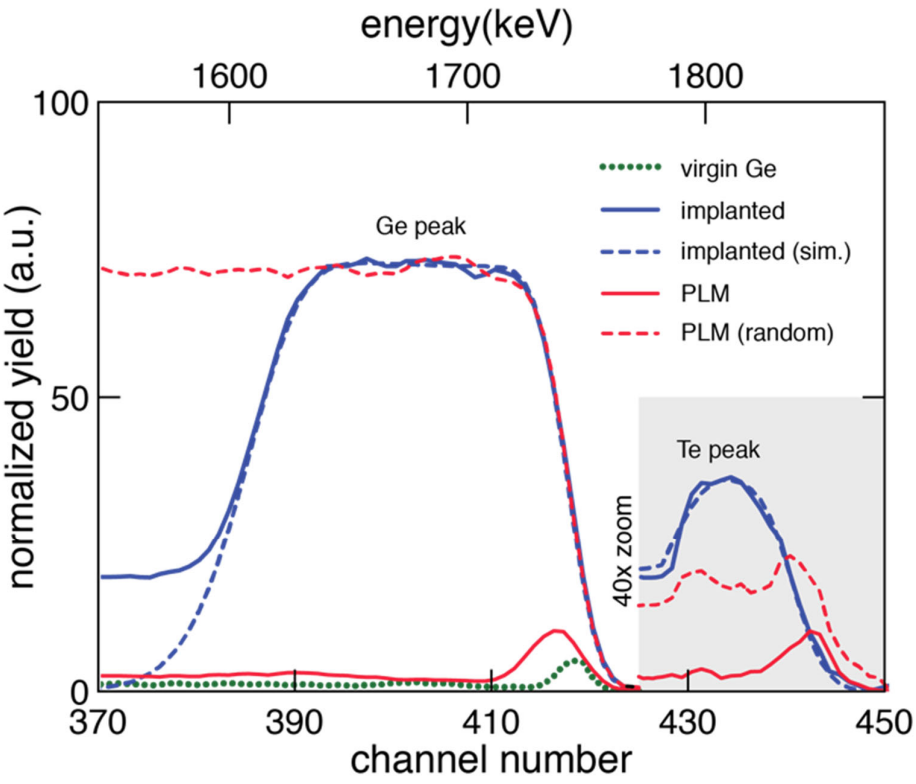

SM Figure 4. Ge:Te RBS spectra. RBS spectra of a virgin-Ge wafer and of Te-implanted high-dose (10^{15} cm^{-2}) samples before and after PLM. All RBS spectra are of channelling-mode measurements, except the random PLM spectrum specifically indicated in the legend and the SIMNRA simulation to obtain the implanted-amorphous thickness. The minimum scattering yield of the laser-melted hypedoped Ge:Te sample ($\chi_{min/Ge}$) is very close to that of the virgin Ge wafer, suggesting that the hyperdoped samples after laser-melting are of excellent crystalline quality. At the magnified Te peak, comparing integrations of the channeled (solid black) and random (dashed black) spectra after PLM, indicates that a significant fraction (> 70%) of incorporated Te dopant atoms are substitutional. It is not possible to calculate the exact substitutional fraction since the deep part of the Te profile overlaps the Ge part of the spectra.